

Optical clocks with accuracy validated at the 19th digit

K.J. Arnold^{1,2*†}, M. D. K. Lee^{1†}, Qi Zhao¹, Qin Qichen¹,
Zhao Zhang¹, N. Jayjong¹, M. D. Barrett^{1,3*}

¹Centre for Quantum Technologies, National University of Singapore, 3
Science Drive 2, Singapore, 117543, Singapore.

²Temasek Laboratories, National University of Singapore, 5A
Engineering Drive 1, Singapore, 17411, Singapore.

³Department of Physics, National University of Singapore, 2 Science
Drive 3, Singapore, 117551, Singapore.

*Corresponding author(s). E-mail(s): cqtkja@nus.edu.sg;
phybmd@nus.edu.sg;

[†]These authors contributed equally to this work.

Optical atomic frequency references [1] have far surpassed their microwave frequency predecessors leading to an anticipated redefinition of the SI second. Accuracies now pushing below 10^{-18} open new possibilities in diverse applications such as fundamental tests of physics and relativistic geodesy. Here we report two $^{176}\text{Lu}^+$ single-ion optical clocks, each with fractional frequency uncertainty near 1×10^{-19} , a five-fold improvement over the highest accuracy reported to date. Through direct comparison via correlation spectroscopy, we demonstrate a relative frequency agreement of $[-2.4 \pm (5.7)_{\text{stat}} \pm (1.0)_{\text{sys}}] \times 10^{-19}$, where ‘stat’ and ‘sys’ indicate the statistical and systematic uncertainty, respectively. This is the first optical reference reporting a comprehensively assessed uncertainty below 10^{-18} that is validated by a same-species comparison of independent systems, simultaneously addressing two key criteria outlined in the international roadmap towards redefinition of the SI second [2]. This significant advance in optical clock accuracy, achieved in practical room-temperature systems, lays a foundation to improve international timekeeping and opens new frontiers for chronometric leveling [3, 4] at the millimeter scale, and tests of fundamental physics [5], including Lorentz invariance [6], general relativity [7], searches for dark matter [8, 9], and variation of fundamental constants [10, 11].

The pursuit of ever-more-accurate optical atomic clocks is motivated by applications ranging from tests of fundamental physics to practical timekeeping and geodesy. As the scientific community seeks consensus on a new standard for redefinition of the SI second [2], it is essential the uncertainty budgets of optical standards are both rigorously evaluated and performance validated through comparisons. While several state-of-the-art optical standards now report evaluated fractional uncertainties below 10^{-18} [12–14], validation has lagged behind with only a few comparisons $\gtrsim 10^{-18}$ [6, 7, 15, 16]. Here we report the first comprehensive characterization of all known sources of systematic uncertainty for two independent $^{176}\text{Lu}^+$ single-ion optical references, each with evaluated systematic uncertainty near 1×10^{-19} , the lowest reported to date, and demonstrate agreement with uncertainty of 5.7×10^{-19} statistically limited after 200 hours of averaging.

This advance in optical clock accuracy is possible due to the relative insensitivity of the $^{176}\text{Lu}^+ {}^1S_0 \leftrightarrow {}^3D_1$ transition to perturbations compared to other leading contenders. In particular, this transition has the lowest sensitivity to black-body radiation (BBR) and magnetic fields of any established clock system, and the large atomic mass makes it less susceptible to motional shifts than lighter atomic species. The complete uncertainty assessment, summarized in Tab. 1, builds on several recent advances, including an improved method for micromotion compensation [17], evaluation of the quadrupole shift via $^{176}\text{Lu}^+$ microwave spectroscopy [18], and evaluation of background gas collision effects [19].

Demonstration of clock agreement at these extreme levels of precision on practical timescales requires exceptionally low instability, a figure of merit for which single trapped ion optical standards have historically lagged relative to neutral-atom optical lattice clocks [20–23]. As laser stabilization technology steadily improves, extending

optical coherence times to several seconds [24, 25], or eventually minutes, it is possible for single ion clocks to close this instability gap for reference transitions that have long excited state lifetimes, such as for Lu^+ and Yb^+ (E3), and well-controlled systematics. In this work, we employ correlation spectroscopy [26, 27] to compare two $^{176}\text{Lu}^+$ optical references well beyond the coherence time of the laser available in our laboratory. We demonstrate interrogation times up to ten seconds and a comparison instability of $4.8 \times 10^{-16}(\tau/\text{s})^{-1/2}$, nearly a factor of 3 improvement over previous work [16]. Comparing optical references via correlation spectroscopy has $\sqrt{2}$ higher instability than comparing independent clocks, and a factor of two higher instability than an individual clock, for the same interrogation time. It follows that these $^{176}\text{Lu}^+$ systems are currently capable of $\sim 2.4 \times 10^{-16}(\tau/\text{s})^{-1/2}$ clock instability if combined with state-of-the-art laser stabilization technology [28]. This is an improvement over the lowest instability demonstrated in an ionic frequency standard [12], and would enable instability below 10^{-18} in less than one day.

By comparison of the two independent atomic references in 11 measurements spanning 200 hours, we obtain a frequency difference of $[-2.4 \pm (5.7)_{\text{stat}} \pm (1.0)_{\text{sys}}] \times 10^{-19}$ demonstrating agreement within the statistical uncertainty and providing strong evidence that all systematic shifts above the 5×10^{-19} level have been accounted for.

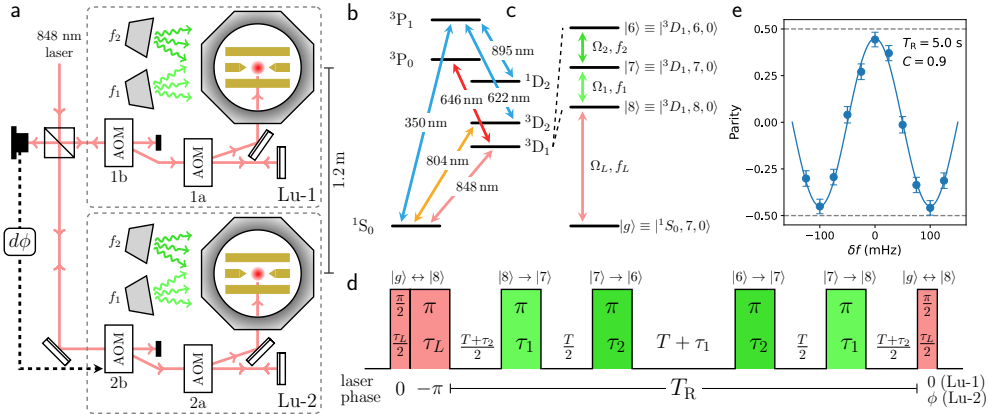


Fig. 1 $^{176}\text{Lu}^+$ correlation spectroscopy (a) Simplified experimental scheme for correlation spectroscopy used to compare Lu-1 and Lu-2. Acousto-optic modulators (AOMs) labeled 1a and 2a control the intensity, frequency, and phase of clock laser pulses delivered to the respective trapped ions, while AOM 2b actively compensates for differential path length fluctuations referenced to retroreflecting mirrors near the viewports of the respective vacuum chambers. Microwaves are delivered by horns external to the vacuum chambers. (b) Atomic level structure of $^{176}\text{Lu}^+$ showing the wavelengths of transitions used. (c) The 848-nm optical clock transition and 3D_1 microwave clock transitions addressed in the clock interrogation sequence. Ω_α and f_α denote the coupling strengths and frequencies for the fields driving the transitions indicated. (d) Clock interrogation sequence for hyperfine-averaged hyper-Ramsey spectroscopy. (e) Parity signal observed for a scan of the optical frequency difference with a Ramsey time $T_R = 5$ s.

Experimental Setup

The experimental setup is summarized in Fig. 1 and is similar to that described in previous work [16]. Single $^{176}\text{Lu}^+$ ions in two independent ion traps, denoted Lu-1 and Lu-2, are compared via correlation spectroscopy. After initialization in the $|8\rangle \equiv |^3D_1, 8, 0\rangle$ state, the ions are simultaneously interrogated with the hyperfine-average (HA) hyper-Ramsey (HR) sequence shown in Fig. 1d. For total Ramsey time T_R much longer than the laser coherence time, the parity $\Pi = \langle \sigma_{z,1} \sigma_{z,2} \rangle$ is given by

$$\Pi(\phi) = \frac{C}{2} \cos(2\pi(\delta\nu - \delta f)T_R + \phi) \quad (1)$$

where $\delta\nu \equiv \nu^{(1)} - \nu^{(2)}$ is the difference in the HA frequencies $\nu^{(k)} = \frac{1}{3}(f_8 + f_7 + f_6)$ for Lu- k , $\delta f \equiv f^{(1)} - f^{(2)}$ is the difference in the HA-equivalent linear combination of laser and microwave frequencies $f^{(k)} = f_L + \frac{1}{3}(2f_1 + f_2)$ used within the interrogation sequence for Lu- k , ϕ is a phase step applied only to the final optical $\frac{\pi}{2}$ pulse for Lu-2, and $C \equiv \max(\Pi) - \min(\Pi) \leq 1$ is the parity fringe contrast. A typical frequency scan demonstrating minimal loss of parity fringe contrast for a Ramsey time $T_R = 5$ s is shown in Fig. 1e.

In previous work [16], the Ramsey time was limited to 700 ms due to a high heating rate in Lu-1. This unusually high heating rate has been resolved by replacing the ion trap with one of the same design. Additionally, the helical resonators for both Lu-1 and Lu-2 were changed to reduce the rf drive frequency Ω_{rf} and obtain higher trap confinement without increasing rf power. For 0.25 W of rf power at $\Omega_{\text{rf}} = 2\pi \times 9.4$ and 11.2 MHz, we obtain secular trapping frequencies of (1134, 1063, 207) kHz and (543, 492, 138) kHz in Lu-1 and Lu-2 respectively, where the weakest confinement corresponds to the axial direction. The measured heating rates are 29.1(1.2) $\mu\text{K/s}$ and 85.4(5.2) $\mu\text{K/s}$ in radial directions, and 73(14) $\mu\text{K/s}$ and 119(17) $\mu\text{K/s}$ in axial directions for Lu-1 and Lu-2 respectively. The combined effect of reduced heating rates and the smaller Lamb Dicke parameters resulting from the increased radial confinement means ion heating is no longer a significant limitation to the interrogation time. The dashed line in Fig. 2a is the simulated contrast loss due to thermal effects.

At the typical operating magnetic field of 0.1 mT in both experiment chambers, we observe the contrast loss as a function of interrogation time shown in Fig. 2a. Although the HA frequency is extremely insensitive to magnetic fields, the individual component transitions are weakly susceptible to magnetic fields via the quadratic Zeeman shifts of the $|^3D_1, F, m_F = 0\rangle$ states. Independent measurements on magnetic sensitive states indicate the ambient magnetic field has flicker instability of 7 nT on the timescales of interest for clock interrogation (~ 1 -100 s). We find the loss of contrast observed is consistent with simulations for magnetic field noise at this level, shown as the solid line in Fig. 2a.

Comparisons of the two independent frequency references are carried out by measuring the parity alternately for $\phi = \pm \frac{\pi}{2}$ and, after N interrogation cycles, steering $\Pi(\frac{\pi}{2}) - \Pi(-\frac{\pi}{2})$ to zero by updating δf . The microwave drive frequencies f_1 and f_2 are identical for both ions and fixed throughout. The frequency difference δf is set by an

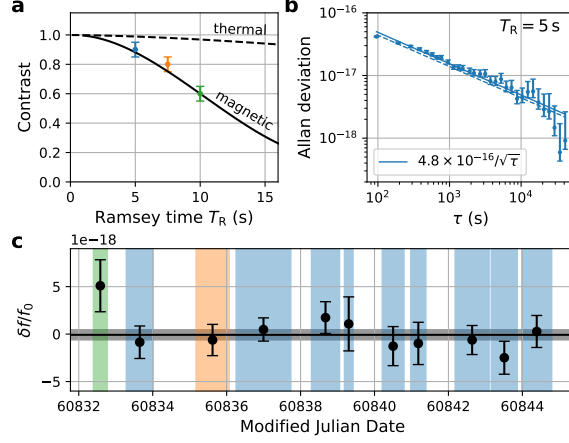


Fig. 2 $^{176}\text{Lu}^+$ comparison results. **a**, Parity contrast inferred from the servo instability (points) compared to the simulated contrast loss due to ion heating (dashed black line) and due to uncorrelated 7 nT magnetic field flicker noise in both chambers (solid black line). **b**, Allan deviation for the longest continuous measurement with $T_R = 5$ s. The dashed line is the projection noise limit for full parity contrast ($C = 1$) and the solid line is observed instability $4.8 \times 10^{-16}(\tau/s)^{-1/2}$ corresponding to $C = 0.9$. **c**, Frequency difference (black points) from 11 measurements with a combined duration of 8.3 days over a 12.4 day interval (67% uptime). Shaded vertical bars show the measurement intervals, with the color indicating Ramsey time for $T_R = 5$ s (blue), 7.5 s (orange), and 10 s (green). The weighted mean frequency difference is $[-2.4 \pm (5.7)_{\text{stat}} \pm (1.0)_{\text{sys}}] \times 10^{-19}$ with reduced chi squared $\chi^2_{\nu} = 0.75$ for 10 degrees of freedom.

acousto-optic modulator (AOM), labelled AOM 2a in Fig. 1a. Two auxiliary measurements are interleaved with the comparison servo: Rabi spectroscopy of the $|g\rangle \leftrightarrow |8\rangle$ optical transition to ensure the 848 nm clock laser is near resonance and measurement of the $|^3D_1, 6, \pm 1\rangle$ Zeeman splitting for each ion using microwave spectroscopy. The Zeeman splitting is used to infer the magnetic field, and feedback is applied to shim coils to compensate for any slow drift. The interrogation time for comparison is typically 84 % of the total duty cycle including the auxiliary measurements.

Results

The results of 11 comparison measurements totaling 200 hours are summarized in Fig. 2c. With the exception of two early measurements taken with Ramsey times of 7.5 s and 10 s, a Ramsey time of $T_R = 5$ s was used. In all cases the observed instability is consistent with the quantum projection noise limit after accounting for the fringe contrast. Fig. 2b shows the Allan deviation of the longest continuous run (37 hours, $T_R = 5$ s) demonstrating an instability of $4.8 \times 10^{-16}(\tau/s)^{-1/2}$. The weighted mean frequency difference of all 11 measurements is $[-2.4 \pm (5.7)_{\text{stat}} \pm (1.0)_{\text{sys}}] \times 10^{-19}$.

We evaluate a total systematic uncertainty of 1.1×10^{-19} for Lu-1, 1.4×10^{-19} for Lu-2, and 9.6×10^{-20} for the difference, with individual contributions summarized in Tab. 1. The only systemic shifts larger than 10^{-18} are the quadratic Zeeman shift and the BBR shift, which is a testament to the insensitivity of $^{176}\text{Lu}^+$ to perturbation. We

Table 1 Clock uncertainty budget. All values are in units 10^{-19} relative to the Lu^+ optical standard frequency. Some effects are common mode which is reflected in the lower uncertainty in the difference. Descriptions for each of these effects can be found in the main text and Methods.

Effect	Lu-1		Lu-2		Difference	
	Shift	Unc.	Shift	Unc.	Shift	Unc.
Quadratic Zeeman	-1383.82	0.15	-1383.82	0.15	0.00	0.04
AC Zeeman (rf)	0.27	0.01	0.52	0.01	-0.24	0.02
AC Zeeman (microwave)	-0.03	0.01	-0.07	0.01	0.05	0.01
Micromotion (excess)	-0.16	0.13	-0.14	0.04	-0.02	0.13
Micromotion (phase)	0	<0.01	-2.42	0.19	2.42	0.19
SODS (thermal)	-3.57	0.29	-5.22	0.33	1.64	0.44
BBR	-13.7	1.0	-13.9	1.1	0.20	0.42
Microwave coupling	0	0.08	0	0.52	0	0.52
Optical coupling	0	<0.01	0	0.04	0	0.04
Residual quadrupole	0.33	0.03	1.35	0.14	-1.02	0.14
AC Stark (848 nm)	0	0.04	0	0.25	0	0.25
AC Quadrupole (rf)	-0.02	<0.01	-0.01	<0.01	-0.01	<0.01
Background collisions	0	0.19	0	0.37	0	0.19
rf synthesis	-	-	-	-	0	0.10
Differential phase chirp	-	-	-	-	-0.05	<0.01
Gravitational	-	-	-	-	-4.31	0.29
Total	-1400.7	1.1	-1403.8	1.4	-1.37	0.96

proceed with a brief discussion on the evaluation of systematic effects with technical details left to the Methods and supported by Extended Data.

A quadratic Zeeman coefficient of $\alpha_z = -4.892\,64(88)\text{ Hz/mT}^2$ measured by comparison at different magnetic fields has been previously reported [16]. In the interest of scientific rigor and since it is the largest systematic shift, α_z was remeasured in both the years 2024 and 2025, with the later measurement data shown in Fig. 3a-b. There is no statistically significant deviation from a quadratic dependence, which highlights the effectiveness of hyperfine averaging operating over a wide range of magnetic fields. The three measurements of α_z are shown in Fig. 3c. We take the weighted mean value of $\alpha_z = -4.893\,27(51)\text{ Hz/mT}^2$ where the statistical uncertainty has been scaled by the square root of the reduced chi-square statistic $\chi_\nu^2 = 1.85$. It is noted the probability $P[\chi_\nu^2 > 1.85] = 0.16$ for the 2-degrees of freedom and so the three measurements of α_z are consistent. For the high accuracy comparison at 0.1 mT, α_z contributes 1.4×10^{-20} to the individual optical references, but this contribution is correlated in the comparison. The uncertainty in the difference of quadratic Zeeman shifts is determined from the magnetic field stability and is less than $< 10^{-20}$ owing to the tracking and active steering of the magnetic fields in both chambers.

The black body radiation shift contributes the largest systematic uncertainty for the individual clocks, at 1×10^{-19} , which is limited by the uncertainty in the dc polarizability [29, 30]. The differential BBR uncertainty is limited by the temperature evaluation. As detailed in the Methods, both experiments operate in a 300.15(20) K

ambient environment and we estimate the temperature increase of the ion traps due to the rf drive from measurements on a test trap of identical construction. We infer a temperature rise of 0.6 K for Lu-1 and 1.6 K for Lu-2, which is also taken as the uncertainty in the temperatures.

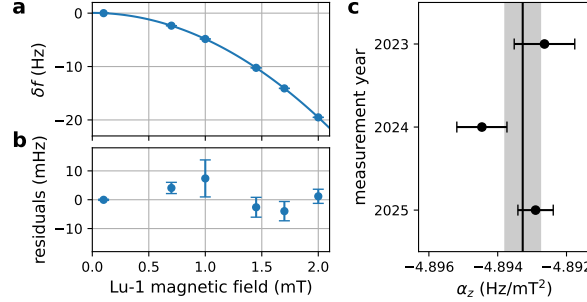


Fig. 3 Measurement of quadratic Zeeman coefficient. **a**, measured frequency difference with Lu-1 operated over a range of field amplitudes and Lu-2 at 0.1 mT. The coefficient α_z is determined from a quadratic fit (solid line). **b**, Residuals with respect to the quadratic fit, which have a reduced $\chi^2_\nu = 0.4$ for 4 degrees of freedom. **c**, Three measurements of α_z over recent years. The 2023 measurement was reported in [16], the 2024 measurement is reported here, and the 2025 measurement is from the data shown in a,b. The vertical line and shaded area represent the combined value of $\alpha_z = -4.89327(51)$ Hz/mT².

Some of the shifts in Tab. 1 are suppressed by the use of long interrogation times: the ac Zeeman shift due to the microwave interrogation pulses, the ac Stark shift due to the 848 nm clock laser, and HA timing errors due to microwave and optical coupling uncertainties. On the other hand, the second-order Doppler shift (SODS) due to thermal motion becomes more significant as the interrogation time is increased due to ion heating. Heating rates for both traps were characterized separately for radial and axial principal axes. At $T_R = 5$ s, the SODS uncertainty is still at the low 10^{-20} level, but would become the largest source of uncertainty for significantly longer interrogation times.

Both the ac magnetic field at the rf trap frequency and the dc electric field gradient are characterized by auxiliary measurements on Lu⁺, in contrast to previous work that used Ba⁺ [31]. The ac magnetic field is inferred by measuring an Autler-Townes splitting on the $|^3D_2, 6, 0\rangle$ to $|^3D_2, 5, 0\rangle$ transition with microwave spectroscopy. The electric field gradient is inferred from the quadrupole shift measured on the 3D_1 microwave transitions, made possible by recent precision measurement of the unperturbed frequencies of the microwave clock transitions [18]. Systematic uncertainty in the quadrupole shift on the HA optical frequency is limited by the uncertainty in the residual quadrupole moment [18, 32].

At the level of accuracy and precision demonstrated in this work, the shift arising from collisions between the ion and the background gas is a potentially important systematic. We have investigated this through both a classical analysis similar to that in [33] and via a quantum treatment given in [34] for which we get agreement from both descriptions. We have shown [19] that the shift can be bounded by the classical Langevin collision rate and a factor that characterizes the decoupling of the

Table 2 Summary of clock accuracy and comparison results

Values are relative to the optical frequencies of the respective standards. All reports, to the best of our knowledge, which satisfy either of the SI redefinition roadmap [2] mandatory criteria of evaluated systematic uncertainty $\leq 2 \times 10^{-18}$ or validation by same-species comparison with an overall uncertainty $\leq 5 \times 10^{-18}$.

Species (Institute)	Year (Ref)	Systematic Unc. [10^{-18}]	Comparison Unc. [10^{-18}]
Yb (NIST)	2018 [15]	6	0.95
Yb ⁺ (PTB)	2019 [6]	2.7	4.2
Al ⁺ (NIST)	2019 [37]	0.94	-
Sr (RIKEN)	2020 [7]	5.5	4.7
Sr (JILA)	2022 [38]	2.0	-
Lu ⁺ (NUS)	2023 [16]	0.6	3.9
Sr (JILA)	2025 [13]	0.81	-
Al ⁺ (NIST)	2025 [12]	0.55	-
Ca ⁺ (SKLC)	2025 [14]	0.46	-
Lu ⁺ (NUS)	This work	0.11	0.57

ion from the clock laser due to the recoil motion. For Lu⁺, this leads to a collision shift of $\pm 6.2 \times 10^{-21}$ nPa⁻¹. Based on collision rates inferred from such decoupling measurements, we infer background pressures of 3 nPa and 6 nPa for Lu-1 and Lu-2 respectively.

Discussion

In summary, we report a full assessment of the systematic uncertainty for two ¹⁷⁶Lu⁺ systems, which, at the level of 1×10^{-19} for both, is the highest accuracy reported to date. An improved evaluation of the dc polarizability as proposed in [35] would immediately reduce the total uncertainty of these existing systems to the level of mid 10^{-20} . Notably these experiments are operated at room temperature in relatively basic linear Paul traps without magnetic shielding, which may be readily developed into transportable optical clocks [36] without compromising accuracy.

The international roadmap for redefinition of the SI second [2] includes as mandatory criteria that optical frequency standards demonstrate relative frequency uncertainty $\leq 2 \times 10^{-18}$ through comprehensively evaluated accuracy budgets, and are validated through frequency ratios that demonstrate agreement of $\leq 5 \times 10^{-18}$. All reports that meet either criteria, to the best of our knowledge, are summarized in Tab. 2. The roadmap mandates same-species, or multiple inter-species, frequency ratio measurements between *independent* institutes. However, *within* institute same-species comparisons are not merely an important first step towards this goal. They are a standard scientific procedure to test the validity of an optical standard's assessments. To the degree that most perturbations are uncorrelated in independent systems, demonstrated frequency agreement gives confidence in the performance of an institute's optical frequency standard and a scientifically sound basis for inter-institute comparisons. Despite this, reports of frequency comparisons at the level $\sim 10^{-18}$ have

so far been few [6, 7, 15, 16]. This work is the first comparison of optical references demonstrating agreement with total uncertainty $< 10^{-18}$.

The comparison stability of $4.8 \times 10^{-16}(\tau/\text{s})^{-1/2}$ is among the best reported for a single-ion standard and the first ion system to make use of such high stability by demonstrating agreement at 5×10^{-19} . The lifetime of 3D_1 is practically indefinite and so substantially longer interrogation times are conceivable but would have to overcome magnetic field noise, ion trap heating, and background gas collisions. Reducing the applied dc magnetic field reduces the sensitivity to magnetic field noise, but introduces challenges due to small Zeeman splittings. Nevertheless, operation at $25 \mu\text{T}$ is possible with changes to our current laser configurations. Based on our assessment here, this should allow interrogation times up to 30 seconds. Much longer coherence times may be possible in the future using magnetic shielding and cryogenics, at the cost of increased complexity in the apparatus.

At the level of performance demonstrated here, measurements are sensitive to the gravitational redshift due to mm-scale height differences. Optical references with uncertainties of 10^{-19} offer a new era of relativistic geodesy beyond state-of-the-art conventional geodetic techniques [4] and the advancement of tests of fundamental physics [5]. Fulfillment of this potential requires rigorous, measurement-based assessment and demonstrated reproducibility of the standards. Below 10^{-18} , lutetium stands alone in this regard.

Methods

Magnetic field stability and servo. Short-term stability of the magnetic field is estimated from measurement of the $|^3D_{1,6,\pm 1}\rangle$ Zeeman splitting with a fast servo attack time (Fig. A1 blue points). Over the range of Ramsey times of interest in this work (~ 1 to 50 seconds), the magnetic field noise shows flicker instability of approximately 7 nT. During comparison measurements the magnetic field is steered to the set point of $B_0 = 0.1$ mT by a compensation coil with a typical servo attack time of $t_{\text{ser}} \approx 80$ s using interleaved measurements of the $|^3D_{1,6,\pm 1}\rangle$ Zeeman splitting. The orange points in Fig. A1 show the field instability inferred from the in-loop measurements of the $|^3D_{1,6,\pm 1}\rangle$ Zeeman splitting which averages down $\propto (t_{\text{ser}}/\tau)$ due to the integration on the field compensation servo. The field instability was checked by interleaved out-of-loop measurements of the $|^3D_{1,8,\pm 1}\rangle$ Zeeman splitting (Fig. A1 green points), which independently confirms the field instability up to the servo projection noise limit $\propto (t_{\text{ser}}/\tau)^{1/2}$ of this tracking servo. This is taken as an upper bound on the magnetic field instability with compensation engaged. The magnetic field contributes uncertainty via the quadratic Zeeman shift of $\frac{\delta\nu_{\text{QZ}}}{\nu_0} = 2\alpha_z B_0 \delta B(\tau) \approx -2 \times 10^{-19} \cdot (\tau/\text{s})^{-1/2}$ beyond the servo attack time.

Detection and background gas collision rates In order to detect background collisions as much as possible and ensure the ions are sufficiently re-cooled before the next experiment cycle, we use the detection sequence shown in Fig. A2a at the end of every Ramsey experiment. The intervals d_i represent adaptive Bayesian state

detection [39] by 646 nm fluorescence. If the ion is detected dark in the initial detection d_0 after the Ramsey sequence, which is $\sim 50\%$ of events, then three attempts are made to shelve on the 848 nm clock transition and detect. The variable 848 nm clock pulse areas are tailored to maximize population transfer even for higher thermally-occupied vibrational n states. The probability of at least one successful shelving is $> 99.5\%$ for the expected thermal distribution accounting for ion heating during the Ramsey dark time T_R . If the ion is not detected bright on any of $d_{0..3}$ then it is assumed that a collision has occurred with sufficient energy transfer to significantly reduce either (i) the coupling on the 848 nm transition or (ii) the 646 nm fluorescence rate. During clock comparison servo operation, if a collision is detected in this way on either Lu-1 or Lu-2, that interrogation cycle is considered invalid and repeated.

If a collision is detected ($d_{0..3}$ all dark), the additional ending sequence shown in Fig. A2a is applied. First a repump pulse (350, 622, and 895 nm) and another detection d_4 is attempted. If bright, this is attributed to a lower energy transfer collision of type (i): sufficient to reduce efficiency of shelving on the clock transition but not detection. If dark, then the collision is of type (ii), energetic enough to disrupt detection. In either case, a cycle of cooling and fluorescence detection with a high threshold, b_i , is repeated until the ion is confirmed bright to ensure the ion is effectively cooled for the next experiment cycle. Fig. A2 b shows the probability of outcomes (i) and (ii) as a function of T_R from which we extract rates $\Gamma^{(i)}$ and $\Gamma^{(ii)}$. To estimate the detectable collision rate Γ , we assume $\Gamma^{(i)} = \frac{1-P_d}{2}\Gamma$ and $\Gamma^{(ii)} = P_d\Gamma$ where P_d is the probability a collision interferes with bright detection, resulting in outcome (ii). Of the lower energy transfer collisions at rate $(1 - P_d)\Gamma$, we assume half are not detected because the ion was in 3D_1 at the end of the Ramsey experiment and half are detected as outcome (i). We infer the collision rates $\Gamma = 1.9 \times 10^{-3} \text{ s}^{-1}$ for Lu-1 and $7.1 \times 10^{-3} \text{ s}^{-1}$ for Lu-2.

After the comparison measurement campaign, additional experiments were performed to estimate the collision rate without the complications introduced by Ramsey spectroscopy. The ions were prepared in the 1S_0 ground state, and after a delay of 5 s, an attempt is made to reshelve and detect using a similar sequence as shown in Fig. A2a. From the probability that all of multiple shelving attempts on the clock transition fail, we directly infer the detectable collision rates $\Gamma = 2.9(3) \times 10^{-3} \text{ s}^{-1}$ for Lu-1 and $6.5(6) \times 10^{-3} \text{ s}^{-1}$ for Lu-2, in reasonable agreement with the rates inferred from the measurement campaign data.

Our extensive analysis of collision shifts in ion-based optical clocks is given in [19]. The collision shift is evaluated with respect to a Langevin collision rate Γ_L , defined as the rate of collisions below a critical impact parameter which result in an inward-spiraling trajectory. As discussed in [19], we estimate Γ_L is a factor of three smaller than the detectable collision rate Γ when accounting for the fraction of glancing collisions that impart sufficient energy to switch off clock laser coupling. We thus estimate Langevin collision rates $\Gamma_L = 1 \times 10^{-3} \text{ s}^{-1}$ for Lu-1 and $2 \times 10^{-3} \text{ s}^{-1}$ for Lu-2, corresponding to 3 nPa and 6 nPa background pressures of molecular hydrogen at 300 K. This is also consistent with pressure gauge readings. An inverted magnetron gauge on Lu-1 reads 4 nPa, and the ion pumps on both chambers read ‘low pressure’ ($< 13 \text{ nPa}$) at the limit of the sensitivity of the ion pump controllers.

Black Body Radiation The differential dynamic polarizability, $\Delta\alpha(\omega)$, for the 848-nm clock transition in $^{176}\text{Lu}^+$ has been well characterized [29, 30]. The BBR shift is given by

$$\frac{\delta\nu_{\text{BBR}}}{\nu_0} = -4.90 \times 10^{-19} \bar{T}^4 (1 + 1.77 \bar{T}^2), \quad (2)$$

where $\bar{T} \equiv T/T_0$ and $T_0 = 300$ K. Over the practical temperature range of 270-330 K, the uncertainty contribution from $\Delta\alpha(\omega)$ is well approximated by $9.8 \times 10^{-20} \bar{T}^4$ [30].

Lu-1 and Lu-2 sit inside an enclosure on the same optical table. The ambient temperature inside the enclosure is continuously monitored by a thermistor that has been calibrated against a Pt100 sensor with 200 mK accuracy. The average temperature in the enclosure over the comparison measurement intervals was $T_e = 300.15\text{ K}$ with maximum deviation from the mean of ± 150 mK (Fig. A3a), less than the calibration uncertainty. Later measurements with multiple calibrated sensors in the enclosure found a stable temperature gradient within the enclosure and the Lu-1 and Lu-2 vacuum chambers had temperature offsets of $-53(10)$ mK and $-246(10)$ mK relative to the central ambient temperature sensor. To estimate the temperature increase of the ion trap due to rf heating, we performed in situ measurements on a third test trap of identical construction to Lu-1 and Lu-2. The trap construction is shown in Fig. A3b. The rf power is delivered from a quarter-wave helical resonator through a single-pin vacuum feedthrough to two of the copper beryllium rod electrodes. The rf and dc electrode rods are held at both ends by ceramic spacers mounted in copper blocks. Iterations of this trap design have used either Macor (as for Lu-1) or Al_2O_3 (as for Lu-2) for the electrode spacer. The test trap was constructed twice with the two different ceramic materials, and the temperature at both end blocks was measured as a function of rf power in vacuum using Pt100 sensors, with the results shown in Fig. A3c. Taking the average of temperature readings from both ends, we observe a temperature increase of 6.6 K/W for the Al_2O_3 spacer and 2.3 K/W for the Macor spacer. In conjunction with the larger temperature rise, we note a significant difference in the loaded quality factor Q of the quarter-wave resonator, from an unloaded Q of 350 to a loaded Q of 240 (70) for Macor (Al_2O_3) test traps, respectively. This is consistent with the difference in the loaded Q observed for Lu-1 and Lu-2, which are 190 and 50 respectively.

The implied dielectric loss tangent for the Al_2O_3 spacers was higher than expected and led us to further investigate with measurements on Al_2O_3 samples from an alternative supplier. However, these samples did not exhibit comparably high dielectric loss, even at relatively low specified purity (95%). It has been reported in literature [40] that the loss tangent of Al_2O_3 varies widely between commercial suppliers, even at high purity ($> 99.5\%$), depending on the nature of the impurities. We suspect the supplied trap spacers are either from a particularly high loss batch or else may not be Al_2O_3 as specified by the manufacturer.

During the comparison measurements, both traps were operated with 0.25 W of rf power, implying a temperature increase of $\Delta T_1 = 0.6$ K and $\Delta T_2 = 1.7$ K for the respective traps. We estimate the BBR temperature of Lu- k as the ambient temperature of the respective vacuum chambers plus ΔT_k with 100% uncertainty assumed, which yields $T_1 = 300.7(0.6)$ K and $T_2 = 301.5(1.6)$ K.

Thermal Second-Order Doppler Thermal motion gives rise to a second-order Doppler shift (SODS) given by

$$\frac{\delta\nu_{\text{SODS}}}{\nu_0} = -\frac{\langle v^2 \rangle}{2c^2} = -\frac{k_B}{2mc^2} (4T_{\text{rad}} + T_{\text{ax}}) \quad (3)$$

where T_{rad} and T_{ax} are the average temperatures during the Ramsey interrogation for the radial and axial principal axes, respectively. Eq. (3) assumes equal contributions from the secular motion and intrinsic micromotion (IMM) for the two radial principal axes, which is valid when the confinement is predominately ponderomotive [41]. Axial confinement is predominately due to the static potential and so only secular motion contributes.

The initial temperatures and heating rates are determined by measuring the temperature immediately after Doppler cooling and after a fixed 1 s delay. The axial temperature is measured by fitting the thermal dephasing of Rabi flopping on the 804 nm E2 transition. Although the 804 nm laser wave vector is at 45° with respect to the ion trap axis and has a projection onto all principal axes, the radial modes have sufficiently low thermal occupation \bar{n} and a small Lambe-Dicke parameter η that they contribute negligibly to the thermal dephasing. From the weighted mean of three measurements over the course of the campaign, we find the initial temperatures $T_{\text{ax},0} = 190.5(5.9) \mu\text{K}$ for Lu-1 and $189.6(4.7) \mu\text{K}$ for Lu-2 and heating rates $\frac{dT_{\text{ax}}}{dt} = 73(14) \mu\text{K/s}$ for Lu-1 and $119(17) \mu\text{K/s}$ for Lu-2, summarized in Fig. A5. The average temperature during the Ramsey experiment is given by $T_{\text{ax}} = T_{\text{ax},0} + \frac{dT_{\text{ax}}}{dt} \frac{T_{\text{R}}}{2}$.

The radial temperatures are measured by spectroscopy on the secular motion sidebands using the 804 nm E2 transition. The average thermal occupation \bar{n} of one of the radial modes is extracted from the ratio of population transferred on the red and blue sidebands [42]:

$$\frac{P_{\text{red}}(t)}{P_{\text{blue}}(t)} = \frac{\bar{n}}{\bar{n} + 1}. \quad (4)$$

We find an initial \bar{n} which corresponds to the temperatures $T_{\text{rad},0} = 174(26) \mu\text{K}$ in Lu-1 and $161(27) \mu\text{K}$ in Lu-2. These are consistent with the initial axial temperatures to within statistical uncertainty and correspond to approximately three times the Doppler cooling limit. The sideband ratio method is most sensitive for low \bar{n} , so for measuring the radial heating rates we first apply Zeeman-degenerate Raman sideband cooling [43] to prepare in the motional ground state and then measure the sideband ratio after some delay. Fig. A6 shows the results of radial heating measurements in both chambers, which yield radial heating rates $\frac{dT_{\text{rad}}}{dt} = 29.1(1.2) \mu\text{K/s}$ for Lu-1 and $85.4(5.2) \mu\text{K/s}$ for Lu-2.

We estimate the total thermal SOD shift for a Ramsey time T_{R} to be:

$$\begin{aligned} (\text{Lu} - 1) \quad \frac{\delta\nu_{\text{SODS}}}{\nu_0} &= -2.3(3) \times 10^{-19} + T_{\text{R}} \cdot [-2.5(2) \times 10^{-20} \text{s}^{-1}] \\ (\text{Lu} - 2) \quad \frac{\delta\nu_{\text{SODS}}}{\nu_0} &= -2.2(3) \times 10^{-19} + T_{\text{R}} \cdot [-6.0(4) \times 10^{-20} \text{s}^{-1}] \end{aligned}$$

Excess Micromotion The micromotion shift has two components: a SODS due to oscillatory motion and the ac-Stark shift due to the rf electric field. Owing to the very low differential polarizability of the clock transition, the ac-Stark contribution is over two orders of magnitude smaller than the SODS component and therefore negligible. The micromotion amplitude is evaluated using phase-modulated sideband spectroscopy on the 804-nm E2 clock transition [17]. The excess micromotion (EMM) second-order Doppler shift is given by

$$\frac{\delta\nu_{\text{EMM}}}{\nu_0} = - \left(\frac{\Omega_{\text{rf}}}{2ck_{804}} \right) \beta^2 \quad (5)$$

where k_{804} is the wave number of the 804-nm clock transition and β is the modulation depth. Since phase-modulated sideband spectroscopy is sensitive to the phase of the micromotion, we distinguish between two quadrature components $\beta = \beta_m + i\beta_p$, where β_m is the excess micromotion due to displacement by stray fields, and β_p is due to a phase shift between rf-electrodes which we are not able to compensate. Intrinsic micromotion (IMM) is accounted for separately with the thermal second-order Doppler shift.

Following the procedure described in [17], we measure the modulation depth in three orthogonal directions to evaluate $\beta_m^2 = \sum_i \beta_{m,i}^2$. The results of all measurements of $\beta_{m,i}$ taken for both ion traps are shown in Fig. A4a-b, where the open circles are measured before compensating the dc stray field and closed circles immediately after. To estimate the EMM shift for each comparison measurement, we linearly interpolate the $\beta_{m,i}$ measurements, assuming linear growth of the dc stray field between measurements. Fig. A4c shows the EMM shifts evaluated from the time average of β_m^2 over each comparison interval. We estimate an average relative shift of $-1.6(1.3) \times 10^{-20}$ for Lu-1 and $-1.4(0.4) \times 10^{-20}$ for Lu-2.

As reported in [17], β_p is negligibly small for Lu-1. For Lu-2, the three orthogonal components of β_p are measured to be $[2.22(13), 1.43(12), 1.92(13)] \times 10^{-2}$, corresponding to an EMM shift of $-2.42(19) \times 10^{-19}$. β_p was remeasured at the end of the campaign and found to be in statistical agreement with the original measurement.

AC Zeeman (rf) Time-varying magnetic fields give rise to an ac-Zeeman shift, with the dominant contributions coming from currents in the electrodes driven by the rf-trapping potential. The contribution depends on the component of the rf-magnetic field perpendicular to the applied dc field [44]. The clock shift given by

$$\delta\nu_{\text{rf}} = \alpha_{\perp} \langle B_{\perp}^2 \rangle \quad (6)$$

where $\sqrt{\langle B_{\perp}^2 \rangle}$ is the root-mean-square rf magnetic field amplitude perpendicular to the dc field and $\alpha_{\perp} = 0.20 \text{ mHz}/\mu\text{T}^2$ is the sensitivity coefficient after 3D_1 hyperfine averaging [44].

While in previous work B_{\perp} was measured via an Autler-Townes splitting on the Ba^+ clock transition [31], here we use an Autler-Townes splitting on the $\text{Lu}^+ ^3D_2 |6,0\rangle$ to $|5,0\rangle$ microwave transition. The 3D_2 $F = 5$ Landé g-factor, $g_5 = -0.38575750(19)$ [45], is the largest of all 3D_1 and 3D_2 F manifolds and for $\Omega_{\text{rf}} \sim$

$2\pi \times 10$ MHz the linear Zeeman splitting can be brought into resonance with Ω_{rf} at experimentally accessible magnetic fields of $B \lesssim 2$ mT.

The experiment measurement procedure is as follows. Neodymium permanent magnets are used to bias the magnetic field to the required 1.7 mT (2.0 mT) for Lu-1 (Lu-2) respectively. Three pairs of coils are used to fine tune the magnetic field amplitude and optimize the orientation for $|^3D_1, 7, 0\rangle$ state preparation by aligning to a π -polarized 646-nm laser. This ensures the dc magnetic field is aligned in the same direction as during the comparison measurements. From $|^3D_1, 7, 0\rangle$, we transfer sequentially to the $|^3D_1, 8, 0\rangle$ state using a microwave π pulse and then the $|^3D_2, 6, 0\rangle$ state using an 804-nm/848-nm Raman pair. We observe the Autler-Townes splitting by interrogating the 3D_2 $|6, 0\rangle$ to $|5, 0\rangle$ microwave transition with a π pulse for a range of detunings, after which the remaining $|^3D_2, 6, 0\rangle$ population is reshelled to $|^3D_1\rangle$ by Raman transfer for detection.

Following the treatment in [44], the effective Hamiltonian in the rotating wave approximation describing the microwave interrogation is

$$H = \frac{\hbar}{2} \begin{pmatrix} -2\Delta_M & \Omega_M & 0 & 0 \\ \Omega_M & 0 & \Omega_B & \Omega_B \\ 0 & \Omega_B & 2\Delta_1 & 0 \\ 0 & \Omega_B & 0 & -2\Delta_{-1} \end{pmatrix} \quad (7)$$

where Ω_M is the microwave coupling, Δ_M is the microwave detuning, $\Omega_B = \frac{1}{\hbar} \frac{\sqrt{15}}{2} g_5 \mu_B B_{\perp}$ is the coupling between $|^3D_2, 5, 0\rangle$ and $|5, \pm 1\rangle$ states due to the transverse oscillating magnetic field at frequency Ω_{rf} , and

$$\Delta_{\pm 1} = \Omega_{\text{rf}} \pm \omega_{\pm 1} = \Omega_{\text{rf}} + g_5 \mu_B B / \hbar \pm \Delta \alpha B^2 \quad (8)$$

is the detuning of the rf field from the $|5, 0\rangle$ to $|5, \pm 1\rangle$ Zeeman splittings, $\omega_{\pm 1}$. Degeneracy of $\omega_{\pm 1}$ is lifted by the differential quadratic Zeeman shift for which $\Delta \alpha \approx 1.23$ kHz/mT².

Fig. A7a shows the simulated spectrum of the Autler-Townes splittings for the operating parameters of Lu-1 and $\Omega_B = 2\pi \times 3$ kHz. For both Lu-1 and Lu-2, several spectra were taken at a fixed magnetic field in the vicinity of the Autler-Townes splitting, of which three from Lu-1 are shown in Fig. A7b-d. We fit the measured data to simulated spectra to obtain Ω_B . Taking the mean of the Ω_B fit values, with the standard deviation of fit values as the uncertainty, we find $\sqrt{\langle B_{\perp}^2 \rangle}$ to be 0.220(5) μ T and 0.303(4) μ T for Lu-1 and Lu-2, respectively. The rf-drive voltage to the trap is monitored over the campaign and for both Lu-1 and Lu-2 varied by less than 0.5%.

AC Zeeman (microwave) When applying the microwave fields during the Ramsey sequence for hyperfine averaging, there is a probe-induced shift due to the σ_{\pm} polarization components off-resonantly coupling to $m = \pm 1$ Zeeman states. Evaluation of this shift is discussed in detail in the Supplementary Material of [16]. The total

microwave ac-Zeeman shift is given by

$$\delta\nu_\mu = \frac{(\Delta_{1,7} + \Delta_{1,8})\tau_1 + (\Delta_{2,6} + \Delta_{2,7})\tau_2}{T_R}, \quad (9)$$

where $\Delta_{k,F}$ is the shift of $|F, m = 0\rangle$ when microwave coupling Ω_k is on. The microwave field polarizations are characterized by measuring the π times τ_{kq} for the field k and polarization q , at fixed microwave power, from which the shifts $\Delta_{k,F}$ are evaluated as:

$$\begin{aligned} \Delta_{1,8} &= -\frac{7}{9} \frac{\Omega_1^2}{4\omega_7} \left[\left(\frac{\tau_{10}}{\tau_{1+}} \right)^2 - \left(\frac{\tau_{10}}{\tau_{1-}} \right)^2 \right] \\ \Delta_{1,7} &= \frac{\Omega_1^2}{4\omega_8} \left[\left(\frac{\tau_{10}}{\tau_{1+}} \right)^2 - \left(\frac{\tau_{10}}{\tau_{1-}} \right)^2 \right] \\ \Delta_{2,7} &= \frac{\Omega_2^2}{4\omega_6} \left[\left(\frac{\tau_{20}}{\tau_{2+}} \right)^2 - \left(\frac{\tau_{20}}{\tau_{2-}} \right)^2 \right] \\ \Delta_{2,6} &= \frac{4}{3} \frac{\Omega_2^2}{4\omega_7} \left[\left(\frac{\tau_{20}}{\tau_{2+}} \right)^2 - \left(\frac{\tau_{20}}{\tau_{2-}} \right)^2 \right] \end{aligned}$$

where $\omega_F > 0$ is the Zeeman splitting for the hyperfine level F .

This shift is suppressed by ensuring $\tau_k \ll T_R$, balancing the circular polarization components ($\tau_{k+} \approx \tau_{k-}$), and maximizing the π coupling ($\tau_{k0} \ll \tau_{k\pm}$). All microwave horns are mounted on rotation mounts and are tuned, through a combination of translation and rotation, to the condition $\tau_{k+} \approx \tau_{k-}$ as much as possible at the start of the campaign. All τ_{kq} were characterized at three points in the campaign, and the evaluated clock shifts were consistently below 1×10^{-20} .

Quadrupole Shift The hyperfine-averaged residual quadrupole moment has been reported as $\tilde{\Theta} = -2.54(0.25) \times 10^{-4} ea_0^2$ [32]. The residual quadrupole shift, $\delta\tilde{\nu}_Q$, is evaluated by measuring the quadrupole shift, $\delta\nu_{Q,1}$, on the $^3D_1 |7,0\rangle$ to $|8,0\rangle$ microwave clock transition, which are related by

$$\delta\tilde{\nu}_Q = \frac{\tilde{\Theta}}{\frac{8}{5}\Theta(^3D_1)} \delta\nu_{Q,1}, \quad (10)$$

where $\Theta(^3D_1) = 0.63862(74) ea_0^2$ [46]. We measure the microwave transition frequencies for both traps by microwave Ramsey spectroscopy with a 10 s interrogation time. The quadrupole shifts $\delta\nu_{Q,1}$ are inferred using the unperturbed microwave frequencies [28] and accounting for the second-order Zeeman shifts. The residual quadrupole

shifts on Lu-1 and Lu-2 are evaluated to be $3.3(3) \times 10^{-20}$ and $1.35(14) \times 10^{-19}$ respectively. Given the accuracy of the measured unperturbed microwave frequencies [28], the quadrupole shift may be easily suppressed further by setting the magnetic field angle so as to null the microwave quadrupole shifts as much as is required.

Coupling Errors Incorrect microwave and optical pulse durations due to uncertainty in the respective couplings give rise to timing errors in the HA-HR spectroscopy. As derived in the Supplemental Material of [16], the shifts due to microwave coupling errors are given by

$$\delta\nu_k \approx -\frac{1}{T_R} \left(\left(\frac{\Delta_k \tau_k}{\pi} \right)^2 + \left(\frac{\pi q_k}{2} \right)^2 \right) \quad (11)$$

where Δ_k is the microwave detuning, τ_k is the microwave π pulse duration, and q_k is the fractional error in the microwave coupling for the $k = 1, 2$ microwave transition.

The optical coupling error is given by

$$\delta\nu_L \approx -\frac{2}{\pi} \frac{\tau_L}{T_R} \Delta_8 \left(\frac{\pi}{2} - 1 \right) q_L \quad (12)$$

where τ_L is the optical π pulse duration, $\Delta_8 = (-2\Delta_2 + \Delta_1)/3$, and q_L is the fractional error in the optical coupling.

These shifts are suppressed for Ramsey times $T_R \gg \tau_L, \tau_k$ as is the case for the comparison experiments reported here. The magnetic field was actively steered to a fixed value in both chambers so the microwave detunings Δ_k are stable and known precisely from the quadrupole shift assessment. The microwave couplings were measured at the beginning, middle, and end of the campaign and found to deviate by less than 0.5%, with the exception of Ω_2 on Lu-2, which drifted by 1.5% over the campaign. The measured optical couplings were within a 1% range for Lu-1 and within 2.5% for Lu-2. The stated percentages are taken as the respective q parameters (coupling uncertainties) in evaluating Eq. (11) and Eq. (12). All coupling systematics are estimated to be $< 1 \times 10^{-19}$.

AC Stark For an optical π time of $\tau_L = \frac{\pi}{\Omega_L} = 4$ ms, the ac Stark shift on the $|g\rangle$ to $|8\rangle$ optical transition when interrogating with the 848-nm laser is approximately $\Delta_S = 2\pi \times 25$ Hz. In the absence of additional effects, hyper-Ramsey [47] suppresses the shift to $\frac{2}{\pi T_R} \left(\frac{\Delta}{\Omega_L} \right)^3$, in Hz, where $\Delta = \Delta_{SP} - \Delta_S$ is the error in the frequency step, Δ_{SP} , applied during the optical interrogation pulses. To set the laser frequency step, Δ_{SP} , the ac-Stark shift was measured to better than 1% for both Lu-1 and Lu-2 at the start of the campaign by comparing Rabi and hyper-Ramsey spectroscopy. The value of Δ_{SP} was fixed throughout the campaign, and we bound the uncertainty in Δ to 2% of $|\Delta_S|$ for Lu-1 and 5% of $|\Delta_S|$ for Lu-2 based on the observed variation in the optical couplings. When including the effects of ion heating, hyper-Ramsey schemes present a weak linear dependence on Δ [48]. This linear dependence is evaluated in simulation with the closing Ramsey pulse averaged over a thermal distribution for radial mode occupation. From the measured heating rates and uncertainties in Δ , we evaluate total uncertainties for ac Stark shift to be 3.8×10^{-21} for Lu-1 and

2.5×10^{-20} for Lu-2 for $T_R = 5$ s.

AC Quadrupole (rf) The oscillating rf quadrupole field couples off-resonantly to hyperfine transitions giving rise to an ac quadrupole shift that is not cancelled by hyperfine averaging [49]. We estimate this shift by assuming an ideal linear Paul trap with rf-potential of the form $\Phi(x, y, z) = \epsilon(x^2 - y^2)$ in the principal-axis frame, where the electric field gradient $\epsilon = \frac{m\Omega_{\text{rf}}\omega_r}{e\sqrt{2}}$ is determined by the radial pseudo-potential confinement frequency $\omega_r \approx 2\pi \times 1100$ kHz for Lu-1 and 510 kHz for Lu-2. The magnetic field in both chambers is aligned to approximately $33(3)^\circ$ with respect to the ion trap axis (z). Under these conditions we evaluate [49] a relative clock shift of the HA frequency of -2.0×10^{-21} for Lu-1 and -5.7×10^{-22} for Lu-2.

RF synthesis The rf synthesizers used for the AOMs are based on the chip AD9912 and have ~ 7 μ Hz resolution. This contributes $\sim 1 \times 10^{-20}$ fractional uncertainty, half of the minimum step size, to the comparison servo. The synthesized microwave frequencies, f_1 and f_2 were identical and generated from the same sources for Lu-1 and Lu-2, set to the nearest 1 mHz. All synthesizers are referenced to a common hydrogen maser which is calibrated to $\lesssim 2 \times 10^{-15}$ at the start of the measurement campaign [50]. When realizing a Lu^+ standard as $\nu_0 = f_L + \frac{1}{3}(2f_1 + f_2)$ via HA Ramsey spectroscopy, the microwave frequencies must have accuracy $\frac{\delta f_k}{f_k} \lesssim \frac{\nu_0}{f_k} \frac{\delta \nu_0}{\nu_0}$ to not be a limiting factor. For the optical frequency comparison, any error in maser accuracy is common mode and contributes no uncertainty to the difference. However to practically realize a frequency standard at the level of $\frac{\delta \nu_0}{\nu_0} = 1 \times 10^{-19}$ would require $\frac{\delta f_k}{f_k} \lesssim 3 \times 10^{-15}$. In practice we would anticipate referencing the microwave synthesizers to the optical frequency via a frequency comb, if a suitably accurate independent reference for the microwave sources were not available.

Differential AOM chirp As shown schematically in Fig. 1a, the differential path length is actively stabilized with reference to retroreflecting mirrors near the respective experimental chambers which are near to the table surface and approximately 20 cm below the trapped ions. The differential phase stability is characterized by out-of-loop measurement of the optical phase with the clock beams directed to a common beam splitter instead of the ions, requiring ≈ 2 m of additional unstabilized optical path length. When simultaneously switching on AOMs 1a and 2a, as for the Ramsey pulses in the comparison interrogation sequence, a differential phase chirp is induced by the lock circuitry which is well modeled by a damped harmonic oscillation with 170 mrad amplitude, 70 kHz frequency, and 7 μ s exponential decay time. By straightforward extension of the analysis given in [51], we evaluate a $-4.8(8) \times 10^{-21}$ systematic shift to difference frequency between Lu-1 and Lu-2 for $T_R = 5$ s.

Gravitational redshift The differential redshift between the ions is given by $\frac{g\delta h}{c^2}$ where $g \approx 9.776 \text{ ms}^{-2}$ is the local gravitational acceleration and $\delta h = h_1 - h_2$ is the height difference of the ions. We measure the heights of the ions relative to a laser leveling assembly fixed to the optical table which is precisely aligned to each ion by the same imaging optics used for state detection. We determine the ion heights

$h_1 = 7.44(10)$ mm and $h_2 = 11.41(10)$ mm. Measurements of the table leveling by a precision spirit level with 0.02 mm/m resolution are limited by the table surface flatness but bound the table tilt to <0.2 mm/m. The ion traps are separated by 1.2 m, and table leveling contributes the dominant uncertainty of 240 μ m. The height difference of the ions is evaluated to be $\delta h = -3.97(27)$ mm, corresponding to a $-4.32(29) \times 10^{-19}$ differential shift.

Acknowledgements. This project is supported by the National Research Foundation, Singapore through the National Quantum Office, hosted in A*STAR, under its National Quantum Engineering Programme 3.0 Funding Initiative (W25Q3D0007) and under its Centre for Quantum Technologies Funding Initiative (S24Q2d0009).

Data availability. All data presented and analyzed in this study are available from the corresponding author upon reasonable request.

Code availability. All codes to analyze the data in this study are available from the corresponding author upon reasonable request.

Contributions. K.J.A and M.D.K.L. performed the experiments and independently analyzed the data. K.J.A prepared the manuscript. M.D.B. supervised the project. All authors contributed to the design of the experiment, discussion of results, and revision of the manuscript.

References

- [1] Ludlow, A. D., Boyd, M. M., Ye, J., Peik, E. & Schmidt, P. O. Optical atomic clocks. *Rev. Mod. Phys.* **87**, 637 (2015).
- [2] Dimarcq, N. *et al.* Roadmap towards the redefinition of the second. *Metrologia* **61**, 012001 (2024).
- [3] Lion, G. *et al.* Determination of a high spatial resolution geopotential model using atomic clock comparisons. *Journal of Geodesy* **91**, 597–611 (2017).
- [4] Mehlstäubler, T. E., Grosche, G., Lisdat, C., Schmidt, P. O. & Denker, H. Atomic clocks for geodesy. *Reports on Progress in Physics* **81**, 064401 (2018).
- [5] Safronova, M. *et al.* Search for new physics with atoms and molecules. *Reviews of Modern Physics* **90**, 025008 (2018).
- [6] Sanner, C. *et al.* Optical clock comparison for Lorentz symmetry testing. *Nature* **567**, 204–208 (2019).
- [7] Takamoto, M. *et al.* Test of general relativity by a pair of transportable optical lattice clocks. *Nature Photonics* **14**, 411–415 (2020).

- [8] Kennedy, C. J. *et al.* Precision metrology meets cosmology: improved constraints on ultralight dark matter from atom-cavity frequency comparisons. *Physical Review Letters* **125**, 201302 (2020).
- [9] Filzinger, M. *et al.* Improved limits on the coupling of ultralight bosonic dark matter to photons from optical atomic clock comparisons. *Physical Review Letters* **130**, 253001 (2023).
- [10] Godun, R. *et al.* Frequency ratio of two optical clock transitions in $^{171}\text{Yb}^+$ and constraints on the time variation of fundamental constants. *Physical review letters* **113**, 210801 (2014).
- [11] Huntemann, N. *et al.* Improved limit on a temporal variation of m_p/m_e from comparisons of Yb^+ and Cs atomic clocks. *Physical review letters* **113**, 210802 (2014).
- [12] Marshall, M. C. *et al.* High-stability single-ion clock with 5.5×10^{-19} systematic uncertainty. *Physical Review Letters* **135**, 033201 (2025).
- [13] Aeppli, A., Kim, K., Warfield, W., Safronova, M. S. & Ye, J. Clock with 8×10^{-19} systematic uncertainty. *Physical Review Letters* **133**, 023401 (2024).
- [14] Zhang, B. *et al.* A liquid-nitrogen-cooled Ca^+ ion optical clock with a systematic uncertainty of 4.6×10^{-19} . *arXiv preprint arXiv:2506.17423* (2025).
- [15] McGrew, W. *et al.* Atomic clock performance enabling geodesy below the centimetre level. *Nature* **564**, 87–90 (2018).
- [16] Zhiqiang, Z., Arnold, K. J., Kaewuam, R. & Barrett, M. D. $^{176}\text{Lu}^+$ clock comparison at the 10^{-18} level via correlation spectroscopy. *Science Advances* **9**, eadg1971 (2023).
- [17] Arnold, K. *et al.* Enhanced micromotion compensation using a phase-modulated light field. *Physical Review A* **110**, 033115 (2024).
- [18] Lee, M. D. K. *et al.* Precision measurement of the $^{176}\text{Lu}^+ \ ^3\text{D}_1$ microwave clock transitions. *arXiv preprint arXiv:2510.06814* (2025).
- [19] Barrett, M. & Arnold, K. Analysis of collision shift assessments in ion-based clocks. *arXiv preprint arXiv:2515.05474* (2025).
- [20] Kim, K. *et al.* Atomic coherence of 2 minutes and instability of 1.5×10^{-18} at 1 s in a Wannier-Stark lattice clock. *Physical Review Letters* **135**, 103601 (2025).
- [21] Hinkley, N. *et al.* An atomic clock with 10^{-18} instability. *Science* **341**, 1215–1218 (2013).

- [22] Liu, X.-Y. *et al.* A zero-dead-time strontium lattice clock with a stability at 10^{-19} level. *arXiv preprint arXiv:2509.15100* (2025).
- [23] Oelker, E. *et al.* Demonstration of 4.8×10^{-17} stability at 1 s for two independent optical clocks. *Nature Photonics* **13**, 714–719 (2019).
- [24] Matei, D. *et al.* 1.5 μm lasers with sub-10 mHz linewidth. *Physical review letters* **118**, 263202 (2017).
- [25] Robinson, J. M. *et al.* Crystalline optical cavity at 4 K with thermal-noise-limited instability and ultralow drift. *Optica* **6**, 240–243 (2019).
- [26] Chwalla, M. *et al.* Precision spectroscopy with two correlated atoms. *Applied Physics B* **89**, 483–488 (2007).
- [27] Clements, E. R. *et al.* Lifetime-limited interrogation of two independent $^{27}\text{Al}^+$ clocks using correlation spectroscopy. *Physical Review Letters* **125**, 243602 (2020).
- [28] Lee, D. *et al.* Frequency stability of 2.5×10^{-17} in a Si cavity with AlGaAs crystalline mirrors. *arXiv preprint arXiv:2509.13503* (2025).
- [29] Arnold, K. J., Kaewuam, R., Roy, A., Tan, T. R. & Barrett, M. D. Blackbody radiation shift assessment for a lutetium ion clock. *Nature communications* **9**, 1–6 (2018).
- [30] Arnold, K. *et al.* Dynamic polarizability measurements with $^{176}\text{Lu}^+$. *Physical Review A* **99**, 012510 (2019).
- [31] Arnold, K. J. *et al.* Precision measurements of the $^{138}\text{Ba}^+$ 6s $^2\text{S}_{1/2}$ - 5d $^2\text{D}_{5/2}$ clock transition. *Physical Review Letters* **124**, 193001 (2020).
- [32] Zhiqiang, Z., Arnold, K., Kaewuam, R., Safronova, M. & Barrett, M. Hyperfine-mediated effects in a Lu^+ optical clock. *Physical Review A* **102**, 052834 (2020).
- [33] Hankin, A. M. *et al.* Systematic uncertainty due to background-gas collisions in trapped-ion optical clocks. *Physical Review A* **100**, 033419 (2019).
- [34] Vutha, A. C., Kirchner, T. & Dubé, P. Collisional frequency shift of a trapped-ion optical clock. *Physical Review A* **96**, 022704 (2017).
- [35] Barrett, M. & Arnold, K. An extrapolation method for polarisability assessments of ion-based optical clocks. *New Journal of Physics* **27**, 013005 (2025).
- [36] Grotti, J. *et al.* Geodesy and metrology with a transportable optical clock. *Nature Physics* **14**, 437–441 (2018).

- [37] Brewer, S. M. *et al.* $^{27}\text{Al}^+$ quantum-logic clock with a systematic uncertainty below 10^{-18} . *Physical review letters* **123**, 033201 (2019).
- [38] Bothwell, T. *et al.* JILA SrI optical lattice clock with uncertainty of 2.0×10^{-18} . *Metrologia* **56**, 065004 (2019).
- [39] Myerson, A. *et al.* High-fidelity readout of trapped-ion qubits. *Physical Review Letters* **100**, 200502 (2008).
- [40] Vila, R., Gonzalez, M., Molla, J. & Ibarra, A. Dielectric spectroscopy of alumina ceramics over a wide frequency range. *Journal of nuclear materials* **253**, 141–148 (1998).
- [41] Berkeland, D., Miller, J., Bergquist, J. C., Itano, W. M. & Wineland, D. J. Minimization of ion micromotion in a paul trap. *Journal of applied physics* **83**, 5025–5033 (1998).
- [42] Turchette, Q. A. *et al.* Heating of trapped ions from the quantum ground state. *Phys. Rev. A* **61**, 063418 (2000).
- [43] Qichen, Q. *et al.* Zeeman degenerate sideband cooling. *arXiv preprint arXiv:2508.02026* (2025).
- [44] Gan, H. *et al.* Oscillating-magnetic-field effects in high-precision metrology. *Physical Review A* **98**, 032514 (2018).
- [45] Zhao, Q. *et al.* Landé g-factor measurements for the $5d6s\ ^3D_2$ hyperfine levels of $^{176}\text{Lu}^+$. *Physical Review A* **112**, 032808 (2025).
- [46] Kaewuan, R. *et al.* Precision measurement of the 3D_1 and 3D_2 quadrupole moments in Lu^+ . *Physical Review A* **102**, 042819 (2020).
- [47] Yudin, V. *et al.* Hyper-ramsey spectroscopy of optical clock transitions. *Physical Review A* **82**, 011804 (2010).
- [48] Kuznetsov, S. N. *et al.* Effect of trapped-ion heating on generalised ramsey methods for suppressing frequency shifts caused by a probe field in atomic clocks. *Quantum Electronics* **49**, 429 (2019).
- [49] Arnold, K. J., Kaewuan, R., Tan, T. & Barrett, M. Oscillating quadrupole effects in high-precision metrology. *Physical Review A* **99**, 022515 (2019).
- [50] Zhang, Z. *et al.* Absolute frequency measurement of a Lu^+ (3D_1) optical frequency standard via link to international atomic time. *Metrologia* **62**, 035008 (2025).
- [51] Falke, S., Misera, M., Sterr, U. & Lisdat, C. Delivering pulsed and phase stable light to atoms of an optical clock. *Applied Physics B* **107**, 301–311 (2012).

Appendix A Extended Data

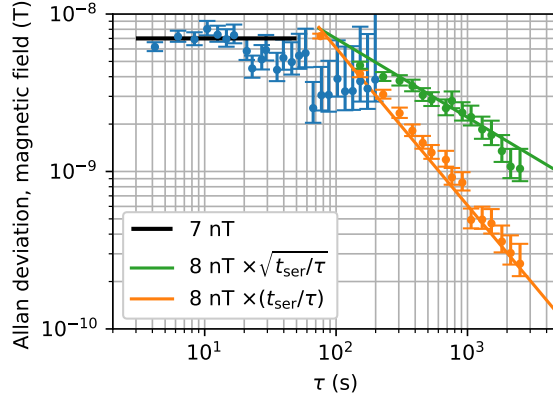


Fig. A1 Magnetic field instability. (blue) measurement of shorter time scale field instability without magnetic field compensation, (orange) instability inferred with magnetic field compensation from in-loop $|^3D_1, 6, \pm 1\rangle$ Zeeman splitting measurements, and (green) independent measurement of magnetic field instability with magnetic field compensation but inferred from out-of-loop $|^3D_1, 8, \pm 1\rangle$ Zeeman splitting measurements.

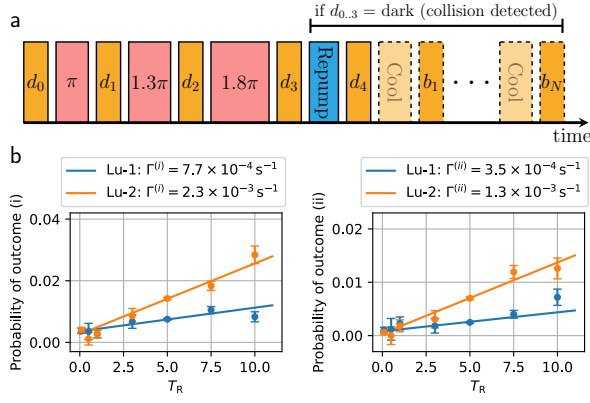


Fig. A2 **a** Detection sequence: (orange) d_i are standard Bayesian state detection and b_i high threshold fixed time detection, (red) 848 nm clock pulses of variable area for shelving, (blue) repump (350 nm, 622 nm, and 895 nm) pulse, and (light orange) laser cooling. **b** Probability of occurrence for outcome (i), first detected bright at d_4 , and outcome (ii), first detected bright on b_i , as a function of Ramsey time for Lu-1 (blue points) and Lu-2 (orange points). Solid lines are linear fits to determine rates.

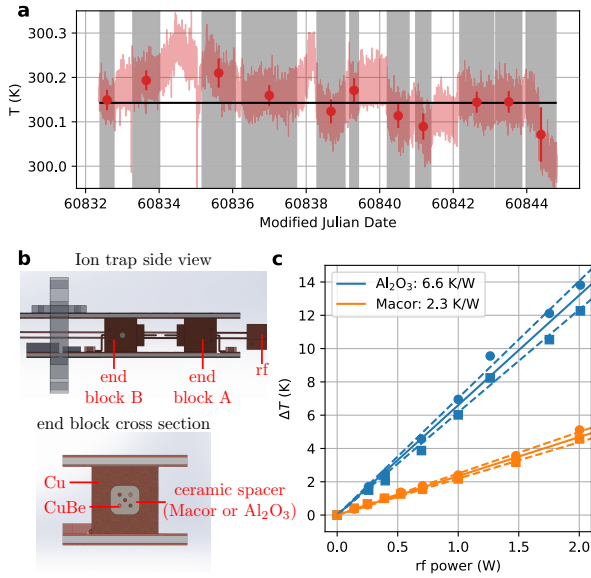


Fig. A3 **a**, Ambient air temperature measured in the clock table enclosure over the duration of the comparison campaign. Red points and error bars indicate the mean and standard deviation of temperature on the comparison measurement intervals. **b**, Ion trap construction. **c**, Measured temperature increase at end block A (squares) and B (circles) for the test trap with Al_2O_3 spacer (blue points) or Macor spacer (orange points).

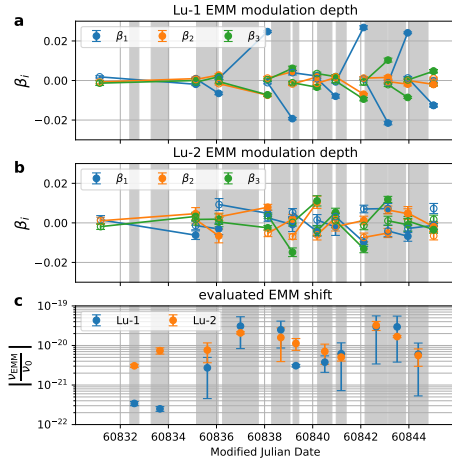


Fig. A4 a-b, EMM modulation depths β_i measured in three orthogonal directions. Solid circles are measurements before compensation, and open circles are measured immediately after compensation. Solid lines are an interpolation over measurement durations. c Total EMM shift evaluated for each comparison measurement interval.

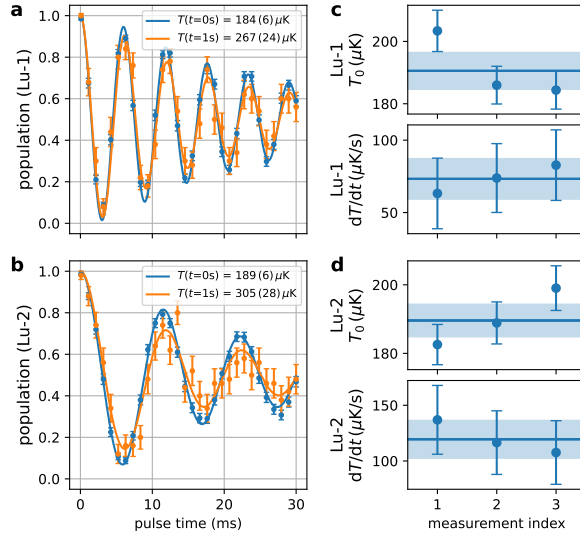


Fig. A5 a-b, A typical measurement of the axial temperature by thermal dephasing after Doppler cooling ($t = 0$) and after a 1 second delay. c-d Initial axial temperature and heating rates from three measurements over the course of the campaign for Lu-1 and Lu-2.

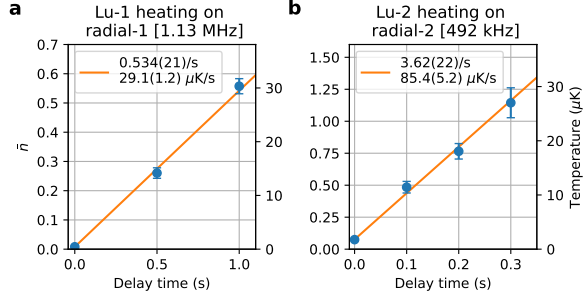


Fig. A6 Radial heating rates for Lu-1 (a) and Lu-2 (b) measured by sideband ratio thermometry after ground state cooling.

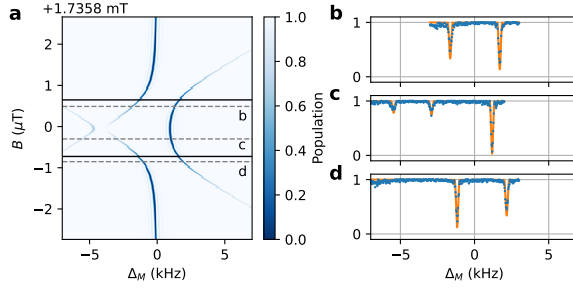


Fig. A7 **a** Simulated Autler-Townes splitting for $\Omega_M = 2\pi \times 100$ Hz and $\Omega_B = 2\pi \times 3$ kHz in Lu-1. Solid black lines denote the Autler-Townes resonance conditions $\Delta_{\pm 1} = 0$. Dashed lines indicate the magnetic fields corresponding to experiment scans b-d. **b-d** Simulation results (orange lines) of Hamiltonian Eq. (7) which are fit to experimental data (blue points) with Ω_B as a free parameter.